

# Spectral Performance Optimization of Small Telescopes For Space Object Detection

GREGORY BADURA,<sup>1</sup> CHRISTOPHER R. VALENTA,<sup>1</sup> BRIAN GUNTER,<sup>2</sup> LUKE RENEGAR,<sup>2</sup> DEVIN WU,<sup>2</sup>

<sup>1</sup>*Georgia Tech Research Institute, Atlanta GA*

<sup>2</sup>*Georgia Institute of Technology, School of Aerospace Engineering, Atlanta, GA.*

## ABSTRACT

Successful tracking and detection of resident space objects (RSOs) in an urban environment such as Atlanta, GA requires optimizing spectral filters for the effects of wavelength dependent atmospheric scattering, material reflectance, and emitted city light pollution. In this study, we perform a multi-spectral optimization for the Georgia Tech Space Object Research Telescope across the visible through infrared spectrum that accounts for atmospheric turbulence, atmospheric transmission, and background sky radiance. The first contribution of this work is the development of a wavelength-dependent performance metric for the detection of RSOs under different atmospheric conditions. The second contribution is the derivation of a simplified model for light pollution that is based on existing astronomy models. This simplified model accounts for double scattering of light and can be used for adding a light pollution component to sky background results that are generated by complex atmospheric simulation tools. The final contribution is the derivation of novel spectral filters that are tuned to the sub-optimal atmospheric seeing conditions of Atlanta, GA and the RSO materials that are considered in this study. While this study is developed for the geographic region of Atlanta, GA and uses simplified reflectance models for RSOs, it can easily be expanded upon and generalized in future studies.

*Keywords:* optical design — atmosphere – light pollution – small telescopes – multi-spectral – optimization

## 1. INTRODUCTION

Detecting, tracking, and identifying resident space objects (RSOs) across geographically diverse locations using small aperture telescopes was proposed to augment larger, more expensive sensors as the number of items in the space catalogue continues to increase (Sabol et al. 2002). While it would be ideal to locate these sensors in prime locations for observation, for a large number of reasons such as meteorological conditions, proximity to urban areas, and geo-political circumstances this choice is not always feasible. As a result, some sensors may be located in areas with less than ideal seeing conditions.

A major challenge of performing tracking and detection within a metropolitan region is the light pollution that accompanies a dense population. When choosing hardware for detection and discrimination of RSOs in a major metro area, it is important to select parameters that are tuned to both the RSO reflectance properties and the urban atmospheric conditions. Astronomers have long realized the benefits of utilizing optical filters to enhance the contrast of their images by using specialized filters to mitigate effects light pollution and enhance the detection of certain nebulae, however this type of analysis is not well documented in the literature for RSO detection.

In order to derive the optimal spectral windows for tracking and detection of RSOs, a wavelength-dependent telescope photometry model must be developed that incorporates the effects of light pollution. Previous works performed by Coder focused on multi-objective design of Raven-class telescopes in the visible spectral region using wavelength-agnostic parameters (Coder & Holzinger 2013, 2016). By performing a multi-spectral optimization that includes visible through infrared wavelengths along with the wavelength dependent nature of optical turbulence, transmission, and sky radiance, among others, ideal spectral filters for RSO detection can be catered to a specific geographic

Corresponding author: Gregory Badura  
gregory.badura@gtri.gatech.edu

location. Moreover, when RSO materials and their characteristic reflectances and emission spectra are identified and integrated into this analysis, increased observation time may result which can provide additional information for the space surveillance network. Additionally, the same type of analysis can be extended to multi-spectral all-sky imaging systems in future works.

This paper derives the optimal spectral window locations for tracking and detection of a number of common RSO materials. The first contribution of this work is the development of a wavelength-dependent performance metric for determining the optimal spectral window for the detection of an RSO material. This performance metric incorporates a number of wavelength dependent parameters including: the light polluted sky background signal, the blurring due to turbulence induced atmospheric seeing, the material spectral signature, and the transmittance of the atmosphere. The second contribution is the derivation of a simplified model for light pollution that is based on existing astronomy models. The final contribution is the derivation of novel spectral filters that are tuned to the sub-optimal atmospheric seeing conditions of Atlanta, GA and the material reflectance properties of the RSOs under consideration.

## 2. METHODS

### 2.1. Derivation of Telescope Limiting Magnitude Objective Function

A method for deriving the limiting detection magnitude of a Raven class telescope was developed in a wavelength-agnostic manner by [Coder & Holzinger \(2013\)](#). In this section, we derive a wavelength-dependent form of this limiting magnitude objective function that allows for the selection of spectral windows that are optimal for RSO detection.

The Signal-to-Noise Ratio (SNR) of an RSO observed by a telescope on the ground can be derived by modeling the photon arrival process on the telescope's CCD as a Poisson process and by assuming a constant background noise spectral signature ([Schildknecht 1994](#)):

$$SNR(\lambda) = \frac{q_{SO}(\lambda)t_{int}}{\sqrt{q_{SO}(\lambda)t_{int} + 2m(\lambda)[q_{dark} + q_{sky}(\lambda)]t_{int} + q_{read}/n^2}}, \quad (1)$$

where  $q_{SO}(\lambda)$  is the wavelength-dependent RSO signal [ $e^-/s/nm$ ],  $q_{dark}$  is the dark noise of the CCD [ $e^-/s$ ],  $q_{sky}(\lambda)$  is the wavelength-dependent sky signature reaching a pixel of the focal plane [ $e^-/s/nm$ ],  $q_{read}$  is the read noise of the sensor electronics [ $e^-/s$ ],  $t_{int}$  is the sensor integration time,  $m(\lambda)$  is the wavelength-dependent number of pixels occupied by the RSO along the focal plane, and  $n$  is a pixel binning factor.

For a moving RSO, the number of pixels occupied by the sensor,  $m(\lambda)$ , grows according to:

$$m(\lambda) = \begin{cases} m_0(\lambda) & \text{if } \omega = 0 \\ m_0(\lambda) + \frac{\sqrt{m_0(\lambda)}\omega t_{int}}{IFOV} & \text{if } \omega \neq 0 \end{cases}, \quad (2)$$

where the instantaneous field of view (IFOV) of a pixel on the sensor focal plane is defined in units of *radians/pixel*,  $m_0(\lambda)$  is the number of pixels initially subtended by the RSO, and the angular velocity of the RSO ( $\omega$  in units of *rad/sec*) assumes that the stationary telescope is operated in stare mode ([Coder & Holzinger 2016](#)).

In this study,  $m_0(\lambda)$  is determined by considering the largest of three metrics of the full-width half maximum (FWHM) of the point spread function (PSF):

- the IFOV of a pixel
- the PSF due to turbulence-induced atmospheric seeing
- the PSF due to diffraction limited seeing

The PSF due to atmospheric seeing is approximately parameterized by the Fried parameter of the system at 500 nm,  $r_0(500\text{ nm})$ , by  $FWHM_{atm}(\lambda) = \lambda/r_0(500\text{ nm})$  ([Fried 1966](#)). The PSF due to diffraction limited seeing is also wavelength dependent, but is instead limited by the diameter of the telescope aperture,  $D_{ap}$ , according to  $FWHM_{diff}(\lambda) = 1.22\lambda/D_{ap}$ . The IFOV of a telescope system of focal length  $f$  and pixel-pitch  $p_{pitch}$  is wavelength agnostic and is purely dependent on the geometry of the system by  $IFOV = 2 \arctan(p_{pitch}/2f)$  ([Budding & Demircan 2007](#)). The wavelength dependent number of initial pixels occupied by an RSO of projected area  $A_{SO}$  at a distance  $R$

to the telescope can then be defined as the maximum of the FWHM divided by the IFOV according to:

$$m_0(\lambda) = \left( \frac{A_{SO}}{R \times IFOV} + \frac{1}{IFOV} \times \max \left\{ \begin{array}{l} \frac{\lambda}{r_0(500 \text{ nm})} \\ \frac{1.22\lambda}{D_{ap}} \\ 2 \arctan \left( \frac{p_{pitch}}{2f} \right) \end{array} \right\} \right)^2 \quad (3)$$

By assuming that the satellites in orbit are non-stationary, Equation 1 can be rewritten in the form:

$$SNR^2 = \frac{q_{SO}^2(\lambda)t_{int}^2}{q_{SO}(\lambda)t_{int} + 2 \left( m_0(\lambda) + \frac{\sqrt{m_0(\lambda)\omega}}{IFOV} \right) [q_{dark} + q_{sky}(\lambda)]t_{int} + q_{read}/n^2} \quad (4)$$

Coder and Holzinger showed that L'Hospital's rule can be applied twice to Equation 4 in order to define the maximum achievable SNR as the integration time goes to infinity (Coder & Holzinger 2013, 2016):

$$SNR_{lim}^2 = \lim_{t \rightarrow \infty} SNR^2 = \lim_{t \rightarrow \infty} \frac{q_{SO}^2(\lambda)}{2 \left( \frac{\sqrt{m_0(\lambda)\omega}}{IFOV} \right) (q_{dark} + q_{sky}(\lambda))} \quad (5)$$

By applying the limit, we derive a final equation for limiting  $SNR$ . This equation defines the maximum achievable SNR in the scenario in which the integration time goes to infinity, accounting for motion induced blurring by the RSO and background signature of the ambient night sky:

$$SNR_{lim} = \frac{q_{SO}(\lambda)}{\sqrt{2 \left( \frac{\sqrt{m_0(\lambda)\omega}}{IFOV} \right) (q_{dark} + q_{sky}(\lambda))}} \quad (6)$$

However, we desire to define a limiting SNR for a detection task and then to determine the spectral windows over where an RSO has an adequate visual magnitude to accomplish the task. For this reason, we rewrite equation 6 in the following manner:

$$q_{SO}(\lambda) = SNR_{lim} \sqrt{2 \left( \frac{\sqrt{m_0(\lambda)\omega}}{IFOV} \right) (q_{dark} + q_{sky}(\lambda))} \quad (7)$$

It can be shown that the signal due to the RSO on the focal plane array (FPA) in units of  $[e^-/s/nm]$  can also be written according to the following equation by treating the sun as a blackbody source:

$$q_{SO}(\lambda) = \tau_{optics}(\lambda)\tau_{atm}(\lambda) \left( \frac{2\pi h c \alpha_{SO}(\lambda) r_{sun}^2}{\pi(1 \text{ AU})^2 \lambda^5 [\exp(hc/\lambda K_B T) - 1]} \right) \left( \frac{A_{SO}}{R^2} \right) \left( \frac{\pi D_{ap}^2}{4} \right) QE(\lambda) \left( \frac{\lambda}{hc} \right), \quad (8)$$

where  $\tau_{optics}$  denotes the wavelength-dependent transmittance of the optics,  $\tau_{atm}(\lambda)$  denotes the wavelength-dependent transmittance of the atmosphere,  $\alpha_{SO}(\lambda)$  denotes the wavelength dependent albedo of the RSO,  $h$  is Planck's constant,  $c$  is the speed of light,  $r_{sun}$  denotes the radius of the sun,  $AU$  denotes an astronomical unit of distance,  $K_B$  is Boltzmann's constant,  $QE(\lambda)$  denotes the spectral quantum efficiency of the FPA sensor,  $D_{ap}$  is the telescope aperture diameter, and  $T$  is the temperature of the sun.

Of particular interest in Equation 8 is the spectral photon flux from the RSO in orbit in units of  $[photons/s/m^2/nm]$ :

$$\phi_{SO}(\lambda) = \left( \frac{2\pi h c \alpha_{SO}(\lambda) r_{sun}^2}{\pi(1 \text{ AU})^2 \lambda^5 [\exp(hc/\lambda K_B T) - 1]} \right) \left( \frac{A_{SO}}{R^2} \right) \left( \frac{\lambda}{hc} \right) \quad (9)$$

By combining Equations 7, 8, and 9 we obtain an expression for the photon flux from an RSO in orbit in terms of the limiting-SNR:

$$\phi_{SO}(\lambda) = \frac{SNR_{lim} \sqrt{2 \left( \frac{\sqrt{m_0(\lambda)\omega}}{IFOV} \right) (q_{dark} + q_{sky}(\lambda))}}{\tau_{optics}(\lambda)\tau_{atm}(\lambda) \left( \frac{\pi D_{ap}^2}{4} \right) QE(\lambda)} \quad (10)$$

The visual magnitude of the RSO,  $m_{v_{SO}}$ , can be written in terms of the photon flux from a magnitude-zero object,  $\Phi_0(\lambda)$ , according to [Shell \(2010\)](#):

$$m_{v_{SO}} = 2.5 \log_{10} \left( \frac{\Phi_0(\lambda)}{\Phi_{SO}(\lambda)} \right), \quad (11)$$

where  $\Phi_0(\lambda)$  [*photons/s/m<sup>2</sup>/nm*] is the photon flux from a magnitude-zero space object, defined by:

$$\Phi_0(\lambda) = \left( \frac{2\pi h c r_{sun}^2}{\pi(1 AU)^2 \lambda^5 [\exp(hc/\lambda K_B T) - 1]} \right) \left( \frac{\lambda}{hc} \right) \times 10^{-0.4 m_{v_0}}, \quad (12)$$

where  $m_{v_0} = 26.4$  is the magnitude of the Vega star which serves as the magnitude-zero source ([Budding & Demircan 2007](#)).

By combining Equations 10, 11, and 12, we now derive a wavelength-dependent form of the limiting visual magnitude from an RSO that is dependent on the telescope and atmospheric parameters:

$$m_{v_{tel}} = 2.5 \log_{10} \left( \frac{\left( \frac{2\pi h c r_{sun}^2}{\pi(1 AU)^2 \lambda^5 [\exp(hc/\lambda K_B T) - 1]} \right) \left( \frac{\lambda}{hc} \right) \times 10^{-0.4 m_{v_0}} \tau_{optics}(\lambda) \tau_{atm}(\lambda) \left( \frac{\pi D_{fp}^2}{4} \right) QE(\lambda)}{SNR_{lim} \sqrt{2 \left( \frac{\sqrt{m_0(\lambda)} \omega}{IFOV} \right) (q_{dark} + q_{sky}(\lambda))}} \right) \quad (13)$$

Examining Equation 13, it is clear that there are three important wavelength-dependent parameters that remain to be modeled: the background signature of the ambient sky onto the focal-plane array ( $q_{sky}(\lambda)$  [*e<sup>-</sup>/s/nm*]), the spectral quantum efficiency ( $QE(\lambda)$  [*e<sup>-</sup>/photon*]), and the atmospheric transmittance of the ambient night sky ( $\tau_{atm}(\lambda)$  [*unitless*]). In Section 3, we outline approaches used to simulate these parameters.

## 2.2. Derivation of RSO Limiting Magnitude Objective Function

Equation 13 only accounts for the telescope optical parameters and seeing parameters of the atmosphere at the site of interest. It does not account for the spectral albedo or bidirectional reflectance distribution function of the object of interest. In order to perform a spectral optimization for a material of interest, it is necessary to define a second objective function that accounts for these RSO reflectance properties. By assuming that the RSO has Lambertian reflectance and using Equations 9, 11, and 12 it can be shown that the per-nm apparent visual magnitude of the RSO due solely to reflectance properties is:

$$m_{v_{RSO}} = 2.5 \log_{10} \left( \frac{\pi 10^{-0.4 m_{v_0}}}{\alpha_{SO}(\lambda) \left( \frac{A_{SO}}{R^2} \right)} \right) \quad (14)$$

In this study, the satellite is assumed to be of a constant material albedo that is oriented at a nadir direction to the satellite of interest. The materials considered are gold, white paint, indium gallium arsenide (InGaAs) solar panels, and silicon solar panels. The material properties were derived from a study on satellite material reflectance performed by [Reyes & Cone \(2018\)](#). The empirically determined spectral albedos of the materials are shown in Figure 1. In this study, it is assumed that the materials occupy the entirety of the surface area  $A_{SO}$  that is oriented nadir to the telescope. This is not a physically realizable assumption, but it allows for the selection of spectral windows that are optimal for the detection of a given satellite material. In future studies, more complex bidirectional reflectance distribution functions (BRDF) will be used to study the manner in which different RSO materials interact with each other through multiple scattering.

## 2.3. Spectral Optimization

The goal of this study is to determine the optimal spectral windows for the detection of RSOs as a function of  $\lambda$ . In this study the objective functions which are being used to determine optimal spectral windows were derived in Equations 13 and 14. However, it should be noted that  $m_{v_{tel}}$  in Equation 13 is the limiting visual magnitude in the context of the telescope and atmospheric parameters. Because the visual magnitude system operates such that RSOs with higher signals have lower values, we seek to maximize  $m_{v_{tel}}$  in our optimization routine. Using the same reasoning, we seek to minimize  $m_{v_{RSO}}$  (or, equivalently, to maximize  $-1 \times m_{v_{RSO}}$ ) from Equation 14. Furthermore,

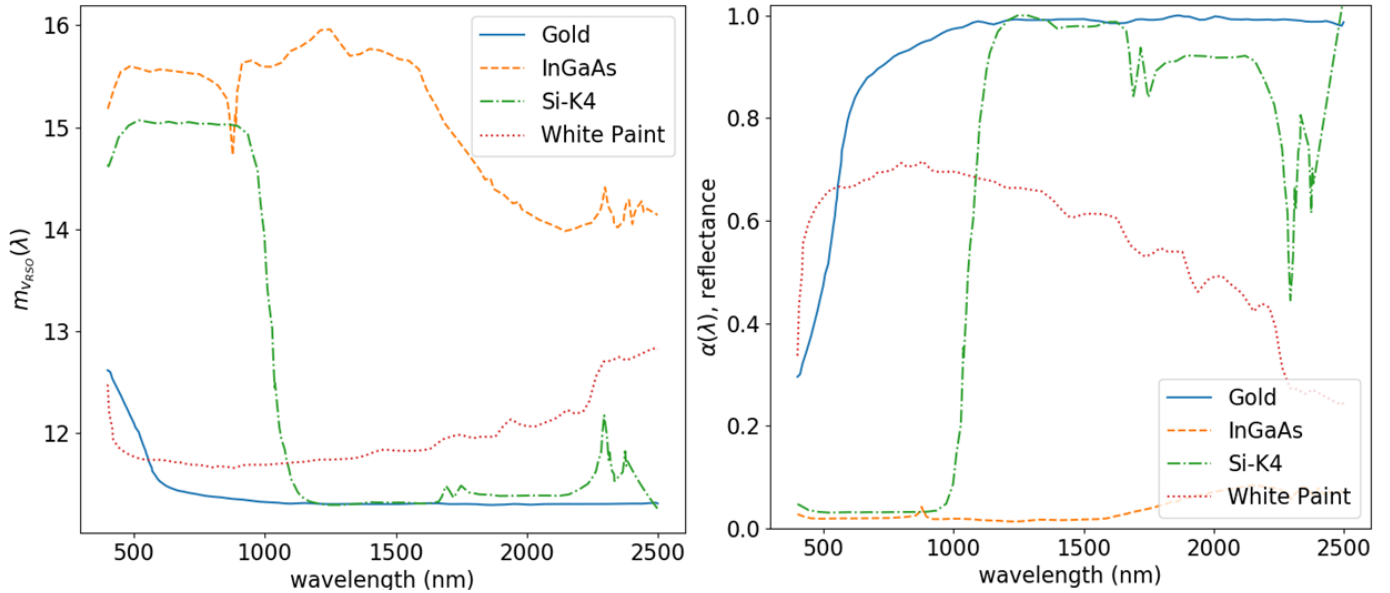


**Figure 1:** Material reflectance curves derived from study performed by (Reyes & Cone 2018) and corresponding apparent visual magnitudes calculated using Equation 14.

each of the functions is normalized in order to ensure that the spectral optimization is not thrown off by the scaled difference between the two objective functions (Arora 2004). Finally, we multiply the retrieved objective function by -1 in order to reframe a maximization problem as a minimization problem. By combining these approaches, the objective function that we seek to minimize as a function of  $\lambda$  can be written as:

$$f_{obj}(\lambda) = -1 \times [norm(-1 \times m_{v_{RSO}}) + norm(m_{v_{tel}})] , \quad (15)$$

where the normalization of the  $j^{th}$  visual magnitude function can be written as:

$$norm(m_j(\lambda)) = \frac{m_j(\lambda) - m_{j_{min}}}{m_{j_{max}} - m_{j_{min}}} \quad (16)$$

It should also be noted that because the objective functions were derived analytically in this study, the objective space is continuous and convex (Coder & Holzinger 2013). Because we are optimizing over wavelength only, approaches such as gradient descent and evolutionary algorithms are not necessary for defining a global local minimum. In future work, this analysis can be extended to consider phase angle dependence and a broader material BRDF database.

### 3. TELESCOPE AND ATMOSPHERIC PARAMETER MODELING

#### 3.1. Spectral Quantum Efficiency of Scientific-Grade Focal Plane Arrays

The spectral quantum efficiency varies significantly depending on the type of sensor being used. In the regions that we consider in our study, two major FPA detectors are typically employed: a silicon-diode charged-coupled device (Si-CCD) FPA and an InGaAs FPA. Cameras employing a Si-CCD FPA have high QE in the ultraviolet to near-infrared (NIR) spectral regions due to the silicon bandgap properties, making them excellent candidates for visible optical imaging. However, Si-CCD sensors often do not provide adequate sensitivity beyond 1100 nm, making them unsuitable for SWIR imaging (Holst & Lomheim 2007). Cooled InGaAs arrays ( $-30^\circ C$  to  $-60^\circ C$ ) operating in ambient temperatures have a dark current noise that is on the order of 100 to 300  $e^-/pixel/s$ , which is much higher than 2 to 4  $e^-/pixel/s$  for a typical Si-CCD array (Princeton Instruments 2019). Deeply cooled ( $-100^\circ C$ ) InGaAs arrays can provide sensitivity over an extended NIR to SWIR range due to a lower bandgap, while maintaining a low dark current that is on the order of Si-CCD's (Hansen & Malchow 2008). In this paper, we assume that the InGaAs arrays are deeply cooled, such that the dark current remains constant over the entire spectral bandwidth of 400 to 2500 nm that is considered in this paper. This assumption can easily be modified for the sake of modeling commercial sensor performance rather than our hypothetical sensor performance.

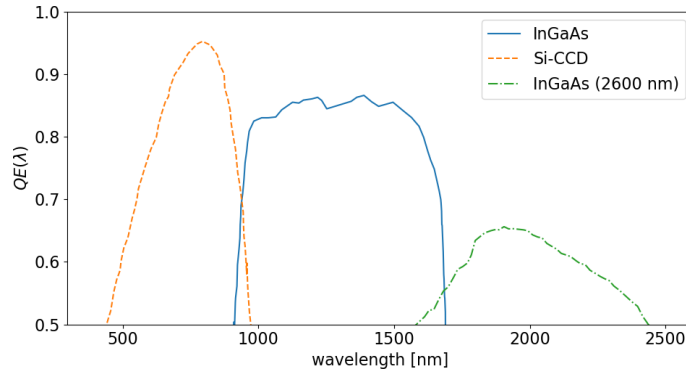


**Figure 2:** Typical quantum efficiency curves of scientific grade cameras: Si-CCD camera (orange) (Princeton Instruments 2019), InGaAs camera sensitive over range of 900 nm to 1600 nm (blue) (Princeton Instruments 2019), and InGaAs camera sensitive up to 2600 nm (green) (Hansen & Malchow 2008).

The performance of different array materials is illustrated by considering the typical QE curves for commercial-off-the-shelf scientific FPA cameras such as those developed by (Princeton Instruments 2019). Typical scientific Si-CCD FPAs used in astronomical imaging rise sharply before peaking in the NIR region of 800 nm, while scientific InGaAs FPAs maintain a near constant QE across a broad region of the SWIR (Princeton Instruments 2019). InGaAs FPAs can also be developed for extended SWIR wavelength sensitivity by shifting the bandgap to longer wavelengths by changing the ratio of Indium to Gallium from a ratio of 53:47 to 82:18, resulting in the detector’s room temperature wavelength response extending out to 2.6 microns (Hansen & Malchow 2008). Quantum efficiency curves for scientific-grade FPA cameras developed from these materials are shown in Figure 2. In this study, the value of  $QE(\lambda)$  used is the maximum of these three curves at a given wavelength. This is meant to model the hypothetical performance of the Georgia Tech Space Object Research Telescope (GT-SORT) in the scenario in which the material of the FPA, and therefore  $QE(\lambda)$ , is the only parameter being modified while the sky background conditions and atmospheric transmittance remains constant.

### 3.2. Atmospheric Modeling of Transmittance and Sky Background Spectra

The MODerate resolution atmospheric TRANsmission program (MODTRAN) is a tool used in the remote sensing community for radiative transfer simulations of different atmospheric scenarios (Berk et al. 1999). It is capable of modeling the atmosphere up to an altitude of 100 km above mean sea-level by treating the atmosphere as 30 discrete layers of different properties. MODTRAN uses empirically measured and theoretically modeled spectra and phase scattering functions of the dominant molecules and aerosols within the atmosphere.

We used MODTRAN’s capabilities in order to model (1) the sky background spectra for a city in the southeastern United States, and (2) the transmittance from an RSO in space downwards onto the city from a nadir direction. In order to model the atmosphere that GT-SORT encounters in Atlanta, we used a Mid-latitude Summer Atmosphere model with a “spring/summer” urban aerosol model and multiple scattering effects. The day of the year used in the simulation was chosen to be 210 (late July), and the time was chosen to be 12 A.M. in local U.S. Eastern time. The moon was used as the source of incident radiance in the simulation with a chosen zenith angle position of  $45^\circ$ . For comparison’s sake, two lunar phase angles were considered in this study:  $0^\circ$  (full-moon) and  $90^\circ$  (half-moon). The city was given a uniform Lambertian albedo of 20% based on previously derived models of city brightness for a telescope positioned within a city (Garstang 1989). The simulation was run using a path from space to the ground in Atlanta (0.32 km above sea level) using these parameters twice: (1) in an upward path in order to model expected downwelled radiance from a nadir look angle due to sky background onto the aperture of GT-SORT, and (2) in a downward path in order to model transmittance along the path from an RSO onto the aperture of GT-SORT. The resulting transmittance and incident radiance curves can be seen in Figure 3. The transmittance curves are nearly identical across the two lunar-phases, suggesting that this parameter is relatively constant across illumination conditions. The major differences in spectral illumination occur in the wavelength range of 400 to 1750 nm due to the spectral blackbody curve of the solar illumination that is being reflected by the moon.

### 3.3. Light Pollution Modeling

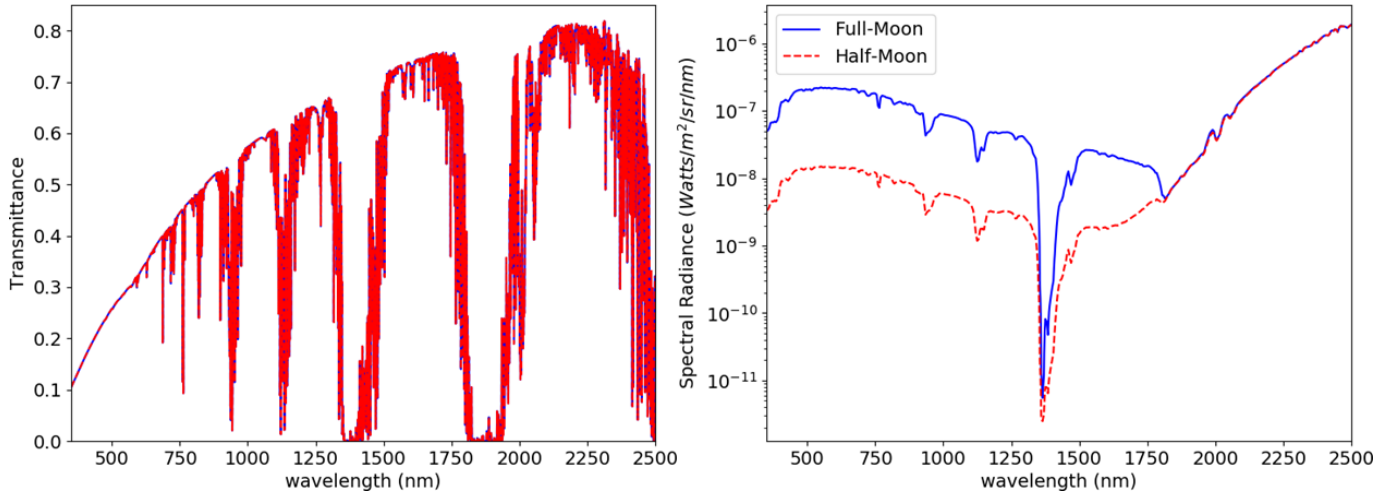


**Figure 3:** The resulting transmittance from Atlanta to space and the downwelled radiance onto the detector in Atlanta for the case of a half-moon (red) and full-moon (blue).

While MODTRAN is appropriate for modeling the transmittance conditions of a city at night, it does not contain any method for simulating light pollution. Studies have shown that the light pollution can degrade detection algorithm performance due to the magnitude and spectral emission features of city light sources (Hänel et al. 2018; Shirkey 2011). For this reason, we adapt a simple model that was originally developed by (Treanor 1973) for approximating light pollution transfer by modeling attenuation of direct and scattered radiance by absorption and scattering losses, and later improved by (Garstang 1989) to allow for aerosol atmospheric density that decreases exponentially with height, and angular dependence of the single scattering albedo and phase scattering functions.

### 3.3.1. Atmosphere Aerosol Model

Our simple atmospheric model consists of a decreasing particle density as a function of increasing vertical propagation distance,  $h$ . The atmospheric layer height can be related to the propagation path distance,  $X$ , over a zenith angle  $\theta$  by  $h = X \cos \theta$ . The atmosphere used in this paper is assumed to consist solely of aerosols and molecules, but can later be extended to account for cloud cover (Shirkey 2011) and dust particles (Garstang 1991). The molecules within the atmosphere are assumed to have a particle density that is solely dependent on  $h$ :

$$N_m(h) = N_m(0)e^{-ch} \quad [1/km^3] \quad (17)$$

where  $N_m(0) = 2.55 \times 10^{24} [km^{-3}]$  is the molecular particle density at mean sea level and  $c = 0.104 km^{-1}$  is the reciprocal scale height of the molecular particle density. The molecules within the atmosphere are assumed to exhibit Rayleigh scattering by particles of experimentally fitted scattering cross section  $\sigma_m = 4.6 \times 10^{-27} [cm^2]$  (Garstang 1989).

The aerosol contribution to the atmosphere is determined by the parameter  $K$ , which measures the ratio of aerosol particle density multiplied by aerosol cross section,  $N_a\sigma_a$ , to molecular  $N_m\sigma_m$  at the city's elevation above sea level,  $H_{city}$ .  $K$  is a measure of the relative importance of aerosols and molecules for scattering light, with a lower value indicating increased clarity of the atmosphere:

$$N_a(0)\sigma_a = 11.11K N_m(0)\sigma_m e^{-cH_{city}} \quad (18)$$

Garstang chose a coefficient 11.11 so that  $K = 1$  experimentally corresponds to aerosol scattering by clear ( $>10 km$  visibility) air at mean sea level (Garstang 1989).

Using this relationship, the aerosol density at an elevation  $h$  can be written using the inverse aerosol scale height  $a = 0.657 + 0.059K [km^{-1}]$ , which is analogous to the parameter  $c$  for molecules:

$$N_a(h) = N_a(0)e^{-ah} = N_a(0)e^{-(0.657+0.059K)h} \quad (19)$$

**Table 1:** Values of vertical optical depth,  $\tau_{OD}$ , and horizontal visibility,  $V_{hor}$ , for the atmospheres considered in light pollution modeling in this study, as defined by the parameter  $K$ .

<b>K</b>	$\tau_{OD}$ [km]	$V_{hor}$ [km]	<b>Classifier Label</b>
1	0.254	25.246	Clear sky
3	0.473	8.879	Moderately Hazy
5	0.623	5.386	Hazy

This atmospheric model can be characterized by using traditional meteorology metrics. The visibility in terms of the horizontal distance distance,  $V_{hor}$ , at which a black object has a contrast of 0.02 relative to the horizon can be shown to be (Garstang 1989)

$$V_{hor} = \frac{3.91}{N_m \sigma_m (1 + 11.778K)} e^{-cH_{city}} \quad (20)$$

Another useful characterization of this simple atmospheric model is the optical depth,  $\tau_{OD}$  of the atmosphere above the observer, which results in a reduction of  $\Delta m = \tau_{OD}/1.0857$  magnitude visibility after traversing through the entire atmosphere (Garstang 1989). This parameter can be used to get a simple approximation of the atmospheric model on the observed visual magnitude of an RSO in orbit:

$$\tau_{OD} = N_m \sigma_m e^{-cH_{city}} \times \left[ \left( \frac{e^{-cH_{city}}}{c} \right) + 11.778K \left( \frac{e^{-aH_{city}}}{a} \right) \right] \quad (21)$$

Table 1 shows values of  $\tau_{OD}$  and  $V_{hor}$  for the values of  $K$  that are considered in this study. These values were chosen for the purpose of simulating light pollution in a clear sky environment ( $K=1$ ), a moderately hazy environment ( $K=3$ ) and a hazy environment ( $K=5$ ) as defined by established meteorological definitions of the horizontal visibility of a hazy atmosphere (Quan et al. 2011; Vautard et al. 2009).

### 3.3.2. Atmosphere Transmittance Losses

Using the atmospheric model defined in Section 3.3.1, Gastang defines the extinction coefficient for the atmosphere as the sum of the molecular and aerosol extinction coefficients over a vertical propagation path of distance  $h$  above the city (Garstang 1989):

$$\kappa(H_{city}, h) = N_m(H_{city} + h)\sigma_m + N_a(H_{city} + h)\sigma_a = N_m(H_{city})\sigma_m (e^{-ch} + 11.11Ke^{-ah}) \quad (22)$$

Using Equation 22, we then derive the transmittance through the atmospheric layers defined by an arbitrary slant path of  $h \cos \theta$ :

$$\tau(H_{city}, h) = \exp \left( \int_0^h -\kappa(H_{city}, h) dh \right) = \exp \left( -N_m(H_{city})\sigma_m \left[ \left( \frac{1 - e^{-ch}}{c \cos \theta} \right) + 11.11K \left( \frac{1 - e^{-ah}}{a \cos \theta} \right) \right] \right) \quad (23)$$

This transmittance model is simplified in that it does not exhibit wavelength-dependence due to the reality that it works with photometric as opposed to radiometric units. In a future study, a wavelength-dependent thresholded-atmosphere approach to modeling light propagation can be incorporated, similar to those employed by the Digital Imaging and Remote Sensing Image Generation (DIRSIG) simulation tool (Ientilucci & Brown 2003).

Finally, assuming that the upwelled illumination from light pollution is either transmitted through the atmosphere or scattered as background illumination, we derive the scattered light contribution as:

$$S(h) = 1 - \exp \left( -N_m(H_{city})\sigma_m \left[ \left( \frac{1 - e^{-ch}}{c \cos \theta} \right) + 11.11K \left( \frac{1 - e^{-ah}}{a \cos \theta} \right) \right] \right) \quad (24)$$

### 3.3.3. City Brightness Contribution

Garstang developed an empirically fitted model for the increase in night sky brightness,  $I_{city}$ , due to a city of population  $P$ . This model assumes that artificial lighting within the city produces an output of  $L$  lumens per head of

population, where  $L$  was also fit to several cities (Garstang 1989). The model assumes that a fraction  $F_{up}$  of the light produced by artificial illumination is directed into upward hemisphere and that the remainder  $(1 - F_{up})$  is directed toward the ground, which has a wavelength-independent albedo  $\alpha_{city}$ . The fraction  $F_{up}$  that is directed in a zenith angle direction upward proportionally to  $\theta^4$ .

$$I_{city} = \frac{LP}{2\pi} (2\alpha_{city}(1 - F_{up}) \cos \theta + 0.554F_{up}\theta^4) \quad [lumens/sr], \quad (25)$$

where the coefficients of 2 and 0.554 are empirically-derived normalizing coefficients (Garstang 1989).

The component of light leaving the city that is transmitted upward ( $I_{\tau_u}$ ) to an altitude of  $h$  above the city can be derived as:

$$I_{\tau_u}(h) = \left( \frac{I_{city}\sigma_m N_m(H_{city})(1 + 11.11K)\tau(H_{city}, h)}{h^2 \cos^2 \theta} \right) (1 + DS(H_{city}, h)) \quad [lumens/sr], \quad (26)$$

where  $DS(h)$  denotes double scattering occurring in an infinitesimal conical solid angle surrounding the forward scattering direction of the city light due to Rayleigh scattering molecular particles (Garstang 1989). Note that this is a simplified model in the sense that it neglects non-forward scattering contributions to sky background brightness.

Within a given layer of the atmosphere of thickness  $\Delta h$ , a portion of light pollution intensity will be scattered and contribute to the overall night sky background brightness. The portion of sky background that is scattered downwards ( $I_{s_d}$ ) and viewed by the sensor due to a given layer can be derived as:

$$I_{s_d}(h, h + \Delta h) = I_{\tau_u}(h) S(h + \Delta h) V_c(h + \Delta h) \Omega_s P(\theta, h), \quad (27)$$

where  $S(h + \Delta h)$  is defined by Equation 24,  $V_c(h + \Delta h)$  is the volume of the conical section associated with the layer,  $\Omega_s$  [sr] is the solid angle of the sensor, and  $P(\theta, h)$  [1/sr/cm<sup>3</sup>] is the phase scattering cross section per unit volume per unit solid angle that was analytically approximated by Garstang (Garstang 1989).

The component of light pollution that will be transmitted back to the sensor in units of [lumens/sr/m] can then be written as:

$$L_L(h, h + \Delta h) = I_{s_d}(h, h + \Delta h) \left( \frac{1}{\pi R_{city}^2} \right) \tau(h) \quad \left[ \frac{lumens}{sr \ m} \right], \quad (28)$$

where  $R_{city}$  is the radius of the city being considered. By integrating through all layers of the atmosphere up to 100 km in order to match the simulation capabilities of MODTRAN, we obtain an estimation of total light pollution,  $L_L^{total}$  that is incident on the sensor due to finite area city.

#### 3.3.4. Conversion to Spectral Radiometric Units

To convert between radiometric and photometric units, we employ the Commission on Illumination's photopic spectral luminous efficiency curve. This curve defines the spectral response of the human eye to various wavelengths of light. The curve provides the normalized efficiency of the human eye over the range of 370 nm to 780 nm. The scaling factor for conversion between radiometric and photometric units is 683 lumens/watt (Judd 1951). Therefore, the desired measure of radiance at the ground due to light pollution for our simple atmosphere model can be approximately derived from  $L^{total} = L_L^{total} \times (1 \text{ Watt}/683 \text{ lumens})$ .

The final step for incorporating the modeled light pollution onto the telescope aperture into our spectral optimization routine is to convert the retrieved radiance to spectral radiance. In order to accomplish this, we use data that was collected on the light distribution in Los Angeles by Shirkey (Shirkey 2011). The light distribution percentage for Los Angeles is shown in Table 2, and the percentage distribution across the modeled spectral ranges of 350-900 nm for these light sources is shown in Figure 4. The incorporation of these signatures in our sky-background model introduces several emission peaks to the relatively smooth spectral signatures of the MODTRAN simulations in Figure 3. These emission peaks are characteristics of the visible-to-NIR sky background signature of major cities including Madrid, Spain (Marin 2009) and Los Angeles, CA (Shirkey 2011), making their inclusion essential for optimizing a telescope for real-world observing.

The spectral radiance onto the sensor can be written in terms of the percentage contribution of the  $i^{th}$  light source,  $C_i$ , and the wavelength dependent normalized spectral distribution of the  $i^{th}$  light source,  $P_i(\lambda)$ :

$$L^{total}(\lambda) = \sum_i C_i P_i(\lambda) L_L^{total} \quad \left[ \frac{Watts}{m^2 \ sr \ nm} \right] \quad (29)$$

**Table 2:** The percentage contribution to the overall city brightness of Equation 25 for Los Angeles in 2011 (Shirkey 2011). This model was used for Atlanta’s light source pollution modeling in this study.

Light Source Type	% Contribution to City Brightness
Mercury Vapor	10
Low Pressure Sodium	5
High Pressure Sodium	55
Metal Halide	20
Incandescent	10

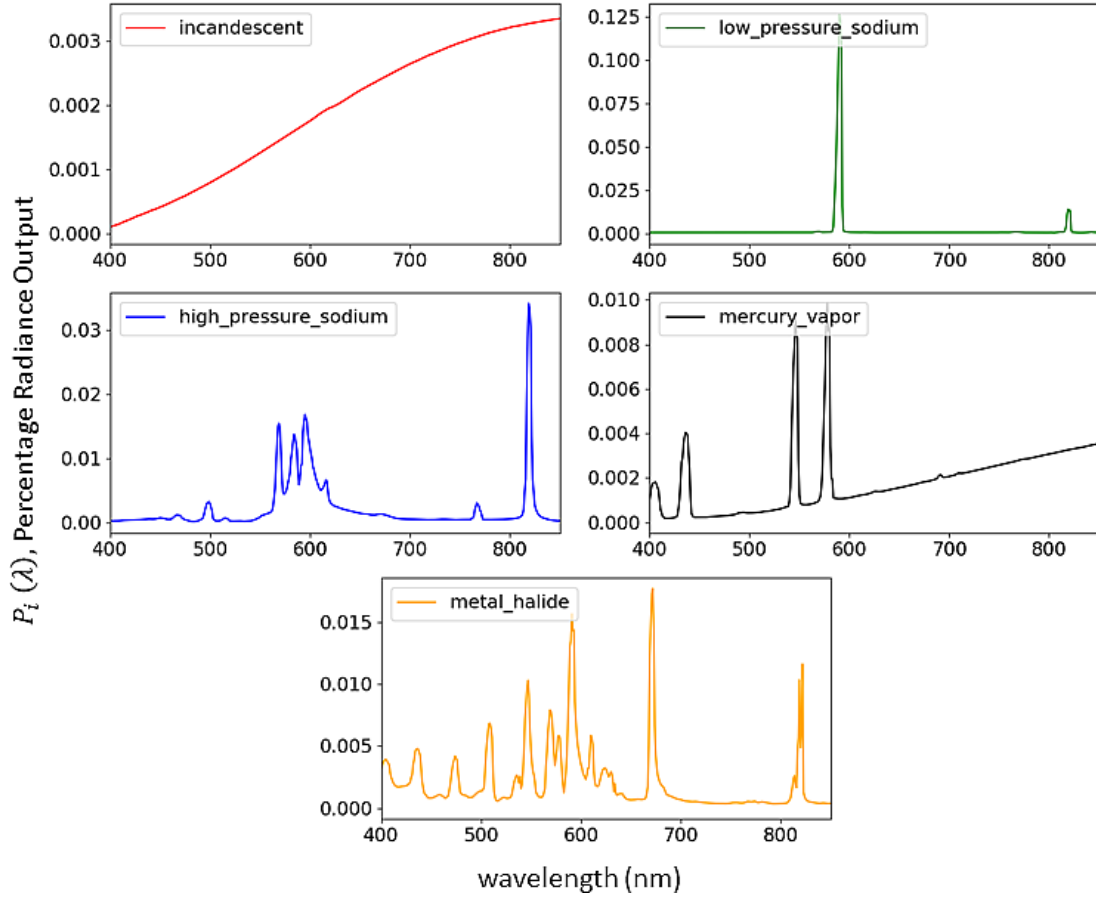


**Figure 4:** The normalized spectral distributions of the light sources used in the modeling of light pollution in Atlanta.

Finally, by assuming that the sky background is an extended source, we can derive the spectral irradiance onto a pixel along the focal plane array (FPA) due to the light pollution background according to the following equation (Coder & Holzinger 2016) for a telescope of  $f_{\#} = f/D_{ap}$ :

$$E^{total}(\lambda) = \frac{L^{total}(\lambda) (1 + 4f_{\#}^2)}{\pi\tau_{optics}} \left[ \frac{Watts}{m^2 nm} \right] \quad (30)$$

The resulting night sky background irradiance can then be obtained by adding the contribution of irradiance onto the FPA due to light pollution, and the typical sky-background which was modeled using MODTRAN. The resulting radiance spectrum derived from this procedure for the case of using a full-moon and a half-moon in our MODTRAN runs is shown in Figure 5. The final calculated background visual magnitude is in the range of 16 to 17, which matches values that were experimentally measured by Coder et al. (2017) in Atlanta, GA in 2013. From these plots, it is clear that the light pollution has a greater effect on the background signature in the case of smaller lunar phase

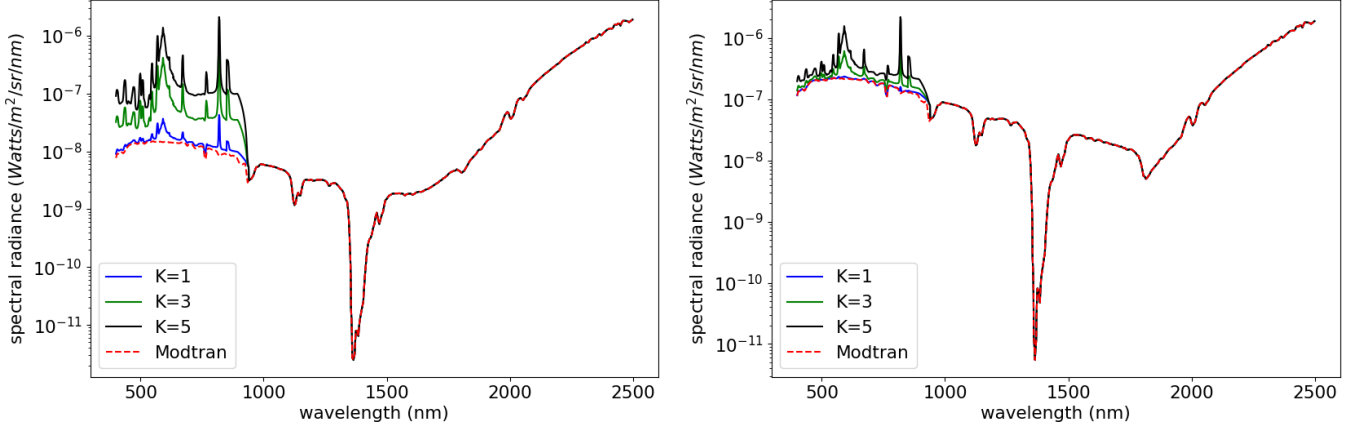


**Figure 5:** The spectral radiance onto the aperture due to the polluted sky background for the case of a half-moon (left) and a full-moon (right).

**Table 3:** Properties used to represent the tracking scenario for the GT-SORT telescope in Atlanta, GA.

Parameter	Symbol	Unit	Value for Scenario
Limiting SNR	$SNR_{lim}$	-	4
Fried Parameter at 500 nm	$r_0(500\text{ nm})$	m	0.025
Dark Current	$q_{dark}$	$[e^-/s/nm]$	2
Aperture Diameter	$D_{ap}$	m	1
Optical Transmittance	$\tau_{optics}$	-	1.0
Pixel Pitch	$p_{pitch}$	$\mu\text{m}$	5.4
Focal length	$f$	m	3
Zenith Angle	$\theta$	degrees	0
F-number	$f\#$	-	6
Astronomical Unit (AU)	$AU$	m	$1.496e^{11}$
RSO Angular Velocity	$\omega$	$rad/sec$	$7.27e^{-5}$
Projected Area of Space Object	$A_{SO}$	$m^2$	1
Lumens per Capita	$L$	lumens/person	2500

angles. In addition, for a clear-sky light pollution model ( $K=1$ ), the radiation scattered by aerosols is minimal. Future investigations should focus on investigating realistic aerosol levels for Atlanta in order to verify our model's fidelity.

Finally, it can be shown that the desired parameter  $q_{sky}(\lambda)$  in units of  $[e^-/s/nm]$  can be defined as:

$$q_{sky}(\lambda) = \frac{L^{total}(\lambda) (1 + 4f\#^2)}{\pi\tau_{optics}} p_{pitch}^2 QE(\lambda) \left( \frac{\lambda}{hc} \right) \quad (31)$$

## 4. RESULTS

### 4.1. Derived Limiting Magnitudes for GT-SORT Telescope

In order to accurately model the optical properties of GT-SORT, we adopt many of the same optical parameters that were defined by Coder (Coder & Holzinger 2016). These parameters are meant to represent the spectrally-independent parameters of performing tracking and detection of RSOs in Atlanta. These are shown in Table 3.

The resulting limiting visual magnitude curve,  $m_{v_{RSO}}$ , from Equation 13 given the telescope and atmospheric parameters for the scenarios outlined above are shown in Figures 6 and 7 for the values of  $K$  considered in this study. Selected standard photometric transmittance filters along with their central wavelength and FWHM bandpasses are shown in Table 4 (Budding & Demircan 2007). These filter sets are plotted as dotted lines in Figures 6 and 7. Using

**Table 4:** Conventional spectral filters used by Astronomers along with the bandwidth and central wavelength of the transmittance curve (Budding & Demircan 2007), and the values of  $m_{v_{SO}}^i$  derived for the optimization functions in this study. Optimal limiting visual magnitude values for a given value of aerosol parameter  $K$  from Equation 18 are shown in bold red text.

Filter Label	Central Band (nm)	Approximate Bandwidth (nm)	$m_{v_{SO}}^i$ for Full-Moon			$m_{v_{SO}}^i$ for Half-Moon		
			K = 1	K = 3	K = 5	K = 1	K = 3	K = 5
B	445	94	11.244	11.175	11.035	13.029	12.114	11.612
V	551	88	11.676	11.547	11.359	12.642	12.405	11.896
R	658	138	12.536	12.376	12.141	13.864	13.104	12.540
I	806	149	<b>12.763</b>	12.631	12.425	<b>14.115</b>	13.409	12.850
Y	1020	120	12.183	12.183	12.183	13.643	13.643	13.643
J	1220	213	12.635	12.635	12.635	14.092	<b>14.092</b>	<b>14.092</b>
H	1630	307	12.672	<b>12.672</b>	<b>12.672</b>	13.927	13.927	13.927
K	2190	390	10.281	10.281	10.281	10.301	10.301	10.301

the  $i^{th}$  spectrally-dependent transmittance curve,  $\tau_{optics}^i(\lambda)$ , we can write the equation for the visual magnitude within the bandpass defined by the transmittance filter,  $m_{v_{SO}}^i$ , by Equation 32.

$$m_{v_{SO}}^i = 2.5 \log_{10} \left( \int_{\lambda_L}^{\lambda_U} \frac{\left( \frac{2\pi h c r_{sun}^2}{\pi(1 AU)^2 \lambda^5 [\exp(hc/\lambda KT) - 1]} \right) \left( \frac{\lambda}{hc} \right) \times 10^{-0.4 m_{v_0}} \tau_{optics}^i(\lambda) \tau_{atm}(\lambda) \left( \frac{\pi D_{ap}^2}{4} \right) QE(\lambda)}{SNR_{lim} \sqrt{2 \left( \frac{\sqrt{m_0(\lambda)} \omega}{IFOV} \right) (q_{dark} + q_{sky}(\lambda))}} d\lambda \right) \quad (32)$$

From the calculated values of Equation 32 shown in Table 4, for a clear sky atmosphere ( $K=1$ ) under both full-moon and half-moon conditions the optimal broadband filter is the *I* band, which extends from the red to near-infrared region. For the case of a moderately hazy ( $K=3$ ) to hazy ( $K=5$ ) atmosphere, increased scattering from light pollution in our optimization routine leads to the shortwave-infrared (SWIR) region being the optimal spectral region for tracking and detection. For the case of a full moon, the optimal filter window is the *H* band, which is centered at 1630 nm. For the case of a half-moon, the optimal filter window is the *J* band, which is centered at 1220 nm. These results indicate that the light pollution and atmospheric scattering of Atlanta render the visible and higher SWIR regions sub-optimal for tracking and detection purposes when haze due to aerosol scattering becomes a factor. Therefore, an InGaAs FPA would be the optimal material for tracking and detection purposes according to our atmospheric modeling approaches. Note that this result assumes that the FPA material being used in the spectral bandpass matches the ideal material for the spectral region from Figure 2. This is a hypothetical scenario which may not be realizable with current InGaAs FPA technology. However, the approach itself can easily be extended to investigate performance of current commercial sensors and all-sky systems. Given that transmitted optical radiation in the atmosphere undergoes Rayleigh scattering, this result makes sense from a conceptual standpoint. However, we have not considered the effects of atmospheric emission in our light pollution model, which could be considerable in Atlanta's climate; future studies should consider this effect to see the effect on sky background signature in the NIR region.

#### 4.2. Optimization Objective Function

The optimization objective function from Equation 15 was calculated for the materials under consideration in this study for the case of Atlanta under illumination by a full-moon and a half-moon for the various atmospheric conditions under consideration in this study. The resulting wavelength dependent optimization function,  $f_{opt}(\lambda)$ , is seen in Figure 8 for the case of a full-moon and in Figure 9 for the case of a half-moon. For each of the RSO materials of interest, lines are plotted for the aerosol  $K$  values considered in this study.

It is apparent that in Figure 8 for the case of a full-moon, there is minimal difference in the optimization objective as the value of  $K$  is increased. For the case of a half-moon in Figure 9, there is a significant increase in  $f_{opt}(\lambda)$  when going from a clear sky ( $K = 1$ ) to a hazy sky ( $K = 5$ ).

It is also apparent from Figures 8 and 9 that the spectral dependence of the function  $f_{opt}(\lambda)$  changes significantly depending on the material under consideration. This is due to the incorporation of the spectral-albedo dependent

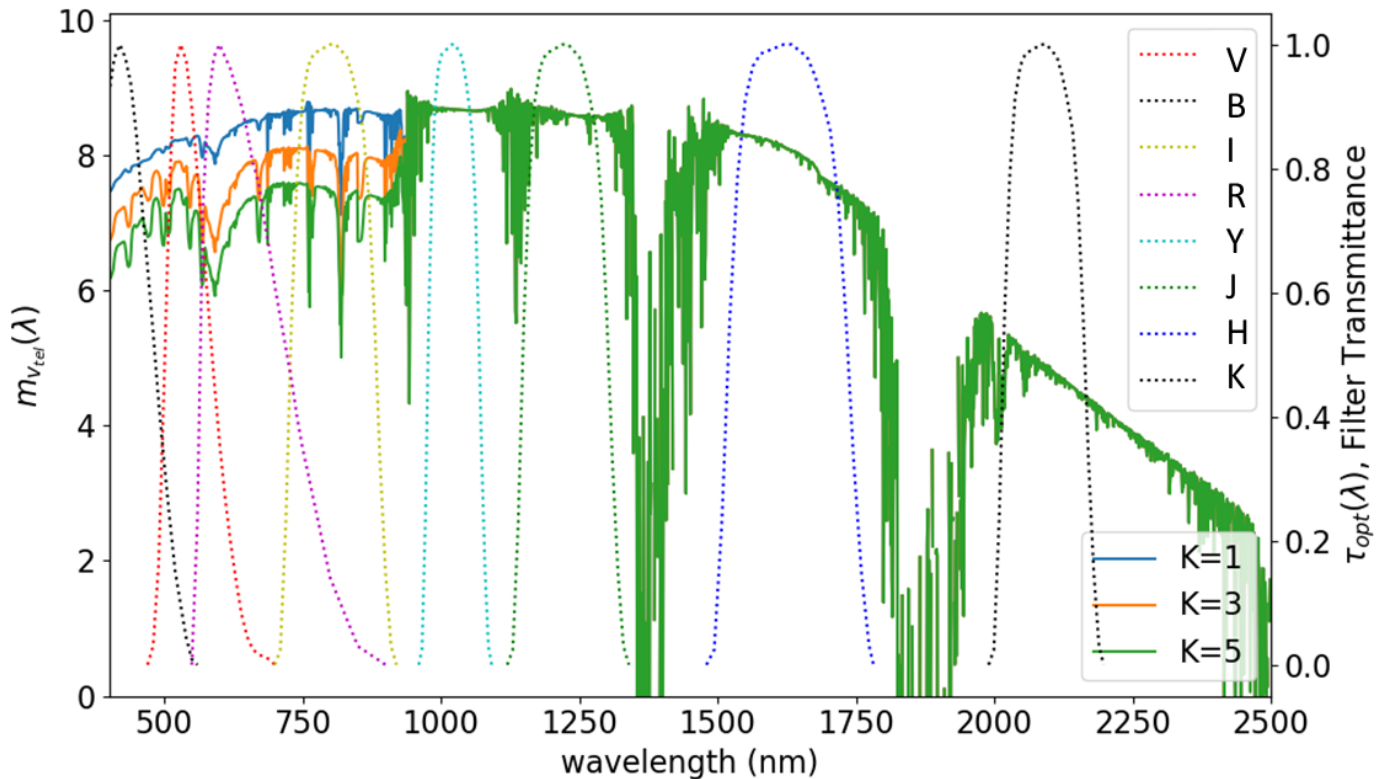


**Figure 6:** The sky background as a function of wavelength in units of magnitude for the case of a half-moon for different atmospheric conditions as defined by  $K$ .

**Table 5:** Optimal bandpass centers for common RSO material detection in the case of illumination by a half-moon.

Material	Filter Bandwidth	Optimal Filter Center Wavelength (nm)		
		K=1	K=3	K=5
Gold	100	1063	1063	1063
	300	1139	1139	1139
InGaAs Solar Panel	100	2080	2080	2080
	300	2110	2110	2110
Si-K4 Solar Panel	100	1225	1225	1225
	300	1198	1198	1198
White Paint	100	836	1015	1015
	300	914	1095	1095

visual magnitude function  $m_{v_{RSO}}$  in Equation 15. For example, the spectral region of 800-950 nm is a viable region for the detection of white paint and gold in both the case of full-moon and half-moon illumination. However, this spectral region is sub-optimal for the detection of Silicon K4 (Si-K4) solar panels due to its lower spectral albedo in this region. These nuances in the spectral behavior of  $f_{opt}(\lambda)$  mean that we can identify optimal spectral windows for the detection of these materials.

We derived optimal spectral bandpass centers for the detection of these materials by performing convolution of a rectangular bandpass with the derived  $f_{opt}(\lambda)$  functions for each material. The minimal value resulting from this series of operations was defined to be the optimal bandpass center wavelength for detection of the given material. The widths of the chosen bandpass windows were 100 nm and 300 nm in order to mimic the narrow-band and wide-band filters defined in the traditional photometric system shown in Table 4. The resulting optimal bandpass centers for the detection of each material are shown in Table 5 for the case of half-moon illumination and in Table 6 for the case of full-moon illumination.

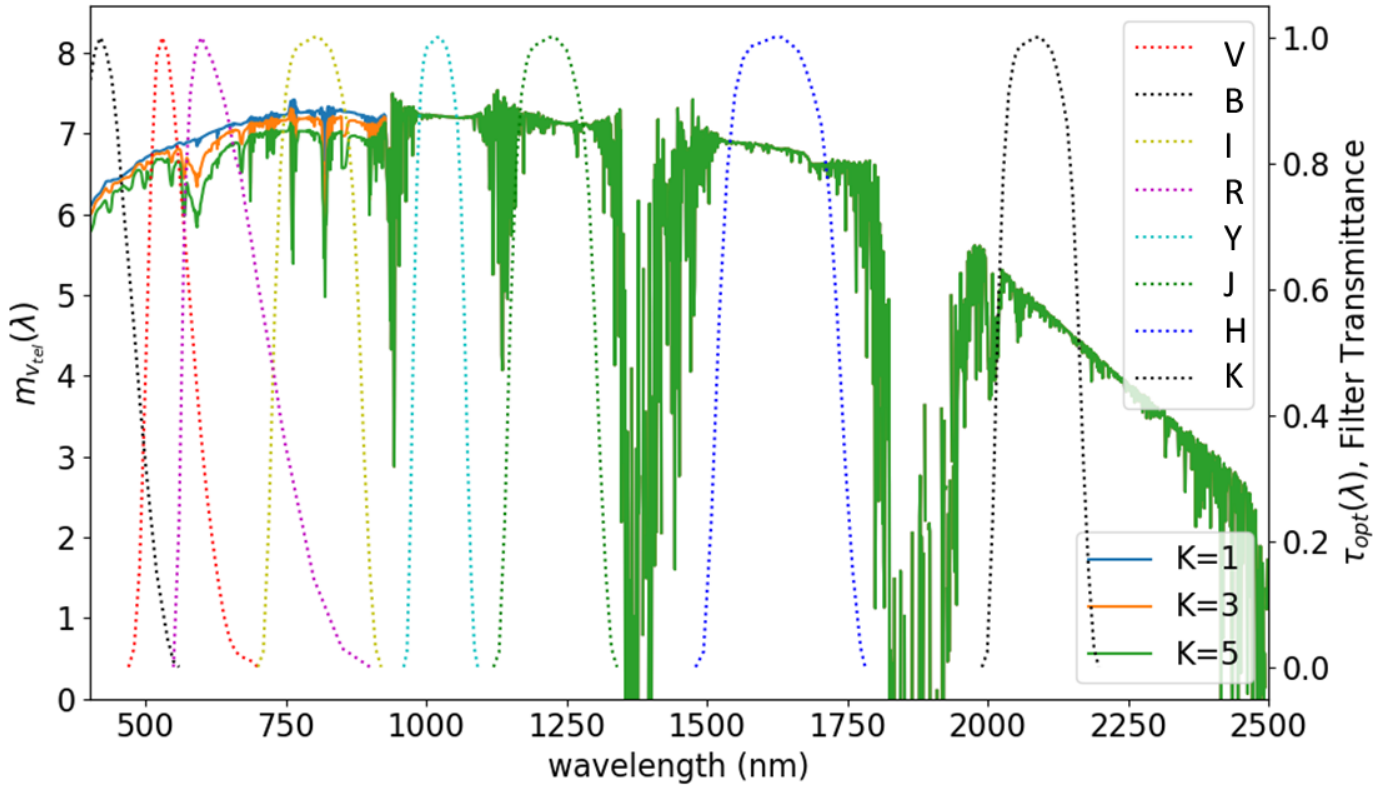


**Figure 7:** The sky background as a function of wavelength in units of magnitude for the case of a full-moon for different atmospheric conditions as defined by  $K$ .

**Table 6:** Optimal bandpass centers for common RSO material detection in the case of illumination by a full-moon.

Material	Filter Bandwidth	Optimal Filter Center Wavelength (nm)		
		K=1	K=3	K=5
Gold	100	1045	1045	1045
	300	1118	1118	1118
InGaAs Solar Panel	100	2075	2075	2075
	300	2110	2110	2110
Si-K4 Solar Panel	100	1225	1225	1225
	300	1198	1198	1198
White Paint	100	836	836	1018
	300	780	914	972

For the case of a gold RSO, the results for the optimal center bandpass are consistent across the case of half-moon illumination and full-moon illumination. The optimal center wavelength of the bandpass changes slightly depending on whether a narrow-bandpass of 100 nm is used or a wide-bandpass of 300 nm is used. In the case of a 100 nm bandpass, it is clear that a bandpass centered at approximately 1050 nm is optimal for all atmospheric conditions under consideration. For the case of a 300 nm bandpass, the center wavelength of 1130 nm is optimal for all atmospheric conditions considered in this study. The Y-band of the Johnson-Cousins photometric system should be sufficient to meet these criteria. However, care must be taken to avoid the absorption feature due to  $H_2O$  in the region of 950 nm that is apparent in the MODTRAN sky background model.

For the case of an InGaAs solar panel material RSO, the optimal bandpass center is consistent across atmospheric and illumination conditions. For the case of a 100 nm and 300 nm bandpass filter, the optimal bandpass center is

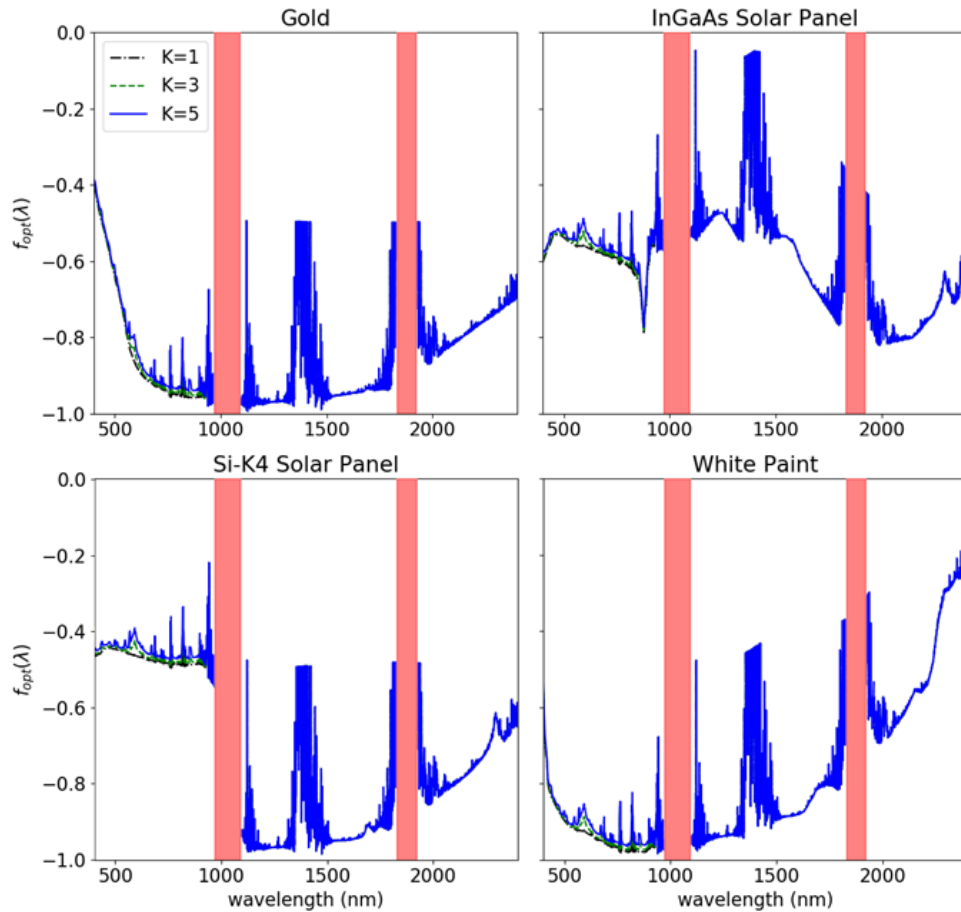


**Figure 8:** The function  $f_{opt}(\lambda)$  from Equation 15 for the case of illumination by a full-moon as  $K$  is varied. Regions where transmittance went to zero due to atmospheric absorption features are marked in red and not considered in the optimization.

at approximately 2100 nm. This indicates that the increased reflectance of gold in the SWIR region outweighs the significantly increased atmospheric blurring in this spectral region.

When detecting a Si-K4 solar panel covered RSO, the optimal bandpass center wavelength is consistent across both lunar phase angle conditions and atmospheric seeing conditions. For the case of a 100 nm bandpass, the optimal center wavelength for detection of a Si-K4 panel RSO is approximately 1225 nm. For the case of a 300 nm bandpass the optimal center wavelength is approximately 1200 nm.

The optimal bandpass center wavelength for detection of white paint varies significantly across atmospheric and lunar illumination conditions. For the case of a 100 nm bandpass filter, the optimal location is in the range of approximately 840 nm to 1000 nm. For the case of a 300 nm filter, the range extends from approximately 800 nm to 1100 nm.

From these limited results, it is clear that the optimal spectral filter for tracking and detection varies considerably depending on the atmospheric conditions in Atlanta and the material that is under consideration. It is also clear that the optimal bandpass centers for detection of the materials considered in this study do not always align with the bandpass centers of the standard photometric filter set for astronomical observations. For example, the optimal center bandpass wavelength for detection of an InGaAs solar panel RSO is approximately in the range of 2100 nm. This is a spectral region that is between the H-band (1550 nm to 1800 nm) and the K-band (2000 nm to 2400 nm) of the standard photometric system. Based on this limited example, it is clear that researchers should consider designing spectral filters outside of the standard photometric system for optimal discrimination of RSOs in tracking and detection purposes. This gap could potentially grow when considering more realistic signature of satellites that are made up of many different materials of varying albedos and bidirectional reflectance distribution functions.

It should be noted that there are several limitations with this analysis. We have assumed that the RSOs are approximately the size of cubesats and are completely coated with the given satellite material under consideration.

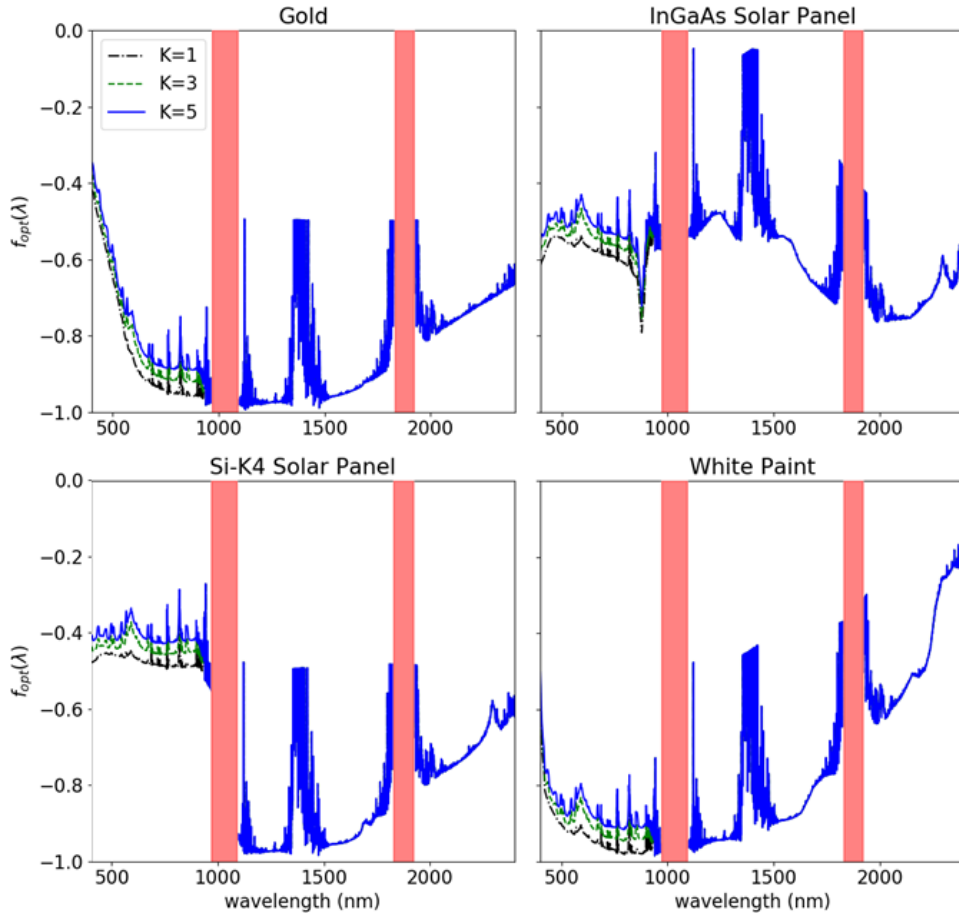


**Figure 9:** The function  $f_{opt}(\lambda)$  from Equation 15 for the case of illumination by a half-moon as  $K$  is varied. Regions where transmittance went to zero due to atmospheric absorption features are marked in red and not considered in the optimization.

Further, we have assumed that the RSO is a Lambertian reflector. Both of these assumptions are clearly not physically realistic, and are only meant to serve as an initial estimate of the optimal spectral regions for detection of the materials. In the future, detailed CAD models with realistic bidirectional-reflectance distribution functions can be considered. Furthermore, we have limited ourselves to nadir viewing. If we considered off-nadir viewing, we would be observing the RSOs through a larger vertical slice of the atmosphere and would therefore likely experience an increased sky background signal. Future studies should also investigate the optimal filter bandpass width that should be used for RSO tracking and detection.

## 5. CONCLUSION

In this study, we performed a multi-spectral optimization for the Georgia Tech Space Object Research Telescope across the visible through infrared spectral that accounts for atmospheric turbulence, atmospheric transmission, and light-polluted background sky radiance. We have also developed a simplified night sky model that has a limited treatment of multiple scattering, has a simplified spectral dependence of scattered radiation, and is based on previous measurements of light source distributions of Los Angeles (Shirkey 2011). It was assumed that we were developing a hypothetical sensor system in which the current Si-CCD FPA could be swapped out with an InGaAs FPA that is deeply cooled and therefore has similar noise characteristics to the Si-CCD array. It was also assumed that the system was observing GEO satellites that were uniformly coated with a single Lambertian reflecting material that maintained a nadir look angle to the telescope system. The initial results suggested that there is merit to developing spectral filter sets that are tuned to discriminate among different RSO materials.

While this study is developed for the geographic region of Atlanta, GA and uses simplified reflectance models for RSOs, it can easily be expanded upon and generalized in future studies. This can include developing realistic

bidirectional reflectance distribution models for RSO materials and developing CAD models of known RSOs. The approach can also be used to determine the detection performance of commercial off-the-shelf telescope systems rather than the hypothetical system considered in this study. In the future, more complicated light pollution models such as the ILLUMINA model developed by Aubé can also be considered in order to improve the atmospheric scattering treatment of upward flux from a city (Aubé & Kocifaj 2012; Aubé & Simoneau 2018).

## 6. ACKNOWLEDGMENTS

This work has been funded by Georgia Tech Research Institute Internal Research and Development (IRAD) funding.

## REFERENCES

- Arora, J. S. 2004, Introduction to optimum design (Elsevier)
- Aubé, M., & Kocifaj, M. 2012, Monthly Notices of the Royal Astronomical Society, 422, 819
- Aubé, M., & Simoneau, A. 2018, Journal of Quantitative Spectroscopy and Radiative Transfer, 211, 25
- Berk, A., Anderson, G. P., Bernstein, L. S., et al. 1999, in Optical spectroscopic techniques and instrumentation for atmospheric and space research III, Vol. 3756, International Society for Optics and Photonics, 348–354
- Budding, E., & Demircan, O. 2007, Introduction to astronomical photometry, Vol. 6 (Cambridge University Press)
- Coder, R., & Holzinger, M. 2013, in Advanced Maui Optical and Space Surveillance Technologies Conference
- Coder, R. D., & Holzinger, M. J. 2016, Acta Astronautica, 128, 669
- Coder, R. D., Jaunzemis, A. D., Mathew, M. V., Worthy, J. L., & Holzinger, M. J. 2017, Journal of Spacecraft and Rockets, 54, 1399
- Fried, D. L. 1966, JOSA, 56, 1372
- Garstang, R. 1989, Publications of the Astronomical Society of the Pacific, 101, 306
- . 1991, Publications of the Astronomical Society of the Pacific, 103, 1109
- Hänel, A., Posch, T., Ribas, S. J., et al. 2018, Journal of Quantitative Spectroscopy and Radiative Transfer, 205, 278
- Hansen, M. P., & Malchow, D. S. 2008, in Thermosense Xxx, Vol. 6939, International Society for Optics and Photonics, 69390I
- Holst, G. C., & Lomheim, T. S. 2007, CMOS/CCD sensors and camera systems
- Ientilucci, E. J., & Brown, S. D. 2003, in Targets and Backgrounds IX: Characterization and Representation, Vol. 5075, International Society for Optics and Photonics, 110–121
- Judd, D. B. 1951, Proceedings of the 12th Session of the CIE, 1951, 1, 11
- Marin, C. 2009, Proceedings of the International Astronomical Union, 5, 449
- Princeton Instruments. 2019, Introduction to scientific InGaAs FPA cameras, Technical Report. <https://www.princetoninstruments.com/userfiles/files/technotes/Introduction-to-scientific-InGaAs-FPA-cameras.pdf>
- Quan, J., Zhang, Q., He, H., et al. 2011, Atmospheric Chemistry and Physics, 11, 8205
- Reyes, J., & Cone, D. 2018, in The Advanced Maui Optical and Space Surveillance Technologies Conference
- Sabol, C., Luu, K. K., Kervin, P., et al. 2002, Advances in the Astronautical Sciences, 112, 397
- Schildknecht, T. 1994, Geod.-Geophys. Arb. Schweiz, No. 49, 49
- Shell, J. R. 2010, Optimizing orbital debris monitoring with optical telescopes, Tech. rep., Air Force Space Innovation and Development Center Schriever AFB CO
- Shirkey, R. C. 2011, Sky Glow from Cities: The Army Illumination Model v2, Tech. rep., Army Research Lab, White Sands Missile Range NM
- Treanor, P. J. 1973, The Observatory, 93, 117
- Vautard, R., Yiou, P., & Van Oldenborgh, G. J. 2009, Nature Geoscience, 2, 115